Ridgelet transform on the sphere

Jason D. McEwen

arXiv:1510.01595v1 [cs.IT] 6 Oct 2015

***Abstract*—We first revisit the spherical Radon transform, also called the Funk-Radon transform, viewing it as an axisymmetric convolution on the sphere. Viewing the spherical Radon transform in this manner leads to a straightforward derivation of its spherical harmonic representation, from which we show the spherical Radon transform can be inverted exactly for signals exhibiting antipodal symmetry. We then construct a spherical ridgelet transform by composing the spherical Radon and scale-discretised wavelet transforms on the sphere. The resulting spherical ridgelet transform also admits exact inversion for antipodal signals. The restriction to antipodal signals is expected since the spherical Radon and ridgelet transforms themselves result in signals that exhibit antipodal symmetry. Our ridgelet transform is defined natively on the sphere, probes signal content globally along great circles, does not exhibit blocking artefacts, does not rely of any *ad hoc* parameters and exhibits an explicit inverse transform. No alternative ridgelet construction on the sphere satisfies all of these properties. Our implementation of the spherical Radon and ridgelet transforms is made publicly available. Finally, we illustrate the effectiveness of spherical ridgelets for diffusion magnetic resonance imaging of white matter fibers in the brain.**

***Index Terms*—Harmonic analysis, spheres, spherical Radon transform, Funk Radon transform, spherical wavelets, spherical ridgelets.**

I. Introduction

WAVELET transforms on the sphere are becoming a standard tool for the analysis of data acquired on a spherical domain. For example, wavelets analyses on the sphere have led to many insightful scientific studies in the fields of planetary science (*e.g.* [1], [2]), geophysics (*e.g.* [3], [4]) and cosmology, in particular for the analysis of the cosmic microwave background (CMB) (*e.g.* [5]–[15]; for a review see [16]), among others. A large body of literature focused on the construction of wavelet methodologies on the sphere now exists [17]–[30]. Of particular note are discrete wavelet frameworks on the sphere, which can support the exact synthesis of signals from their wavelet coefficients in a stable manner, including: needlets [22]–[24]; directional scale-discretised wavelets [25]–[27]; and the isotropic undecimated and pyramidal wavelet transforms [30]. All three of these approaches have been extended to analyse spin signals on the sphere [31]–[37], such as the polarisation of the CMB [38], and to analyse signals defined on the three-dimensional ball formed by augmenting the sphere with the radial line [39]–[42], such as the distribution of galaxies in our Universe [43]. In addition, needlets and scale-discretised wavelets satisfy excellent concentration properties, in terms of quasi-exponential localisation and asymptotic uncorrelation properties [23], [44].

This work was supported by the Engineering and Physical Sciences Research Council (grant number EP/M011852/1).

J. D. McEwen is with the Mullard Space Science Laboratory (MSSL), University College London (UCL), Surrey RH5 6NT, UK.

E-mail: jason.mcewen@ucl.ac.uk

However, the effectiveness of wavelets on the sphere is limited when it comes to representing highly anisotropic signal content, such as lines or curvilinear structures. Directional scale-discretised wavelets on the sphere [25]–[27], [35], [44] go some way to addressing this shortcoming by allowing signal content to be probed not only in scale and position but also in orientation. Furthermore, the steerability property of scale-discretised wavelets means that signal content at any continuous orientation can be probed from a finite set of basis orientations. Nevertheless, geometric properties of structures are not exploited. In Euclidean space, alternative transforms such as ridgelets and curvelets have been devised for such a purpose [45]–[48], which in turn (may) rely on the Radon transform [49], [50].

The spherical Radon transform, also called the Funk-Radon transform, is constructed from the integration of a signal along great circles [51]. The spherical Radon transform finds direct use in practical applications, such as diffusion magnetic resonance imaging (MRI) [52], for example, but is also useful as a building block in the construction of other transforms. In this article we present a novel take on the spherical Radon transform, viewing it as a convolution with a kernel defined by a Dirac delta function in colatitude, such that it is non-zero along the equatorial great circle only. Viewing the spherical Radon transform in this manner helps to aid intuition, which leads to a straightforward derivation of its harmonic action. The harmonic representation of the spherical Radon transform has been presented previously [53]–[55], however the resulting derivations are more complicated. In addition, we show that inversion of the spherical Radon transform is well-posed for signals that exhibit antipodal symmetry. While techniques that attempt to invert the spherical Radon transform are typically approximate [56]–[59], our approach is exact.

The Radon transform may be used as a building block to construct ridgelet and curvelet transforms [45]–[48], [60], which exhibit the geometric structures required to represent highly anisotropic signal content effectively. The planar ridgelet transform is constructed by first performing a Radon transform, which maps singularities along lines to point singularities, followed by a one-dimensional wavelet transform along the slices of the Radon transform. The first-generation curvelet transform is constructed by performing ridgelet transforms on local overlapping blocks [46]. In contrast, second-generation curvelets are constructed from a frequency partition technique [47], [48]. For a review of ridgelet and curvelet transforms in Euclidean space see [61].

First-generation ridgelets and curvelets were constructed on the sphere in [30]. However, these constructions are built on the HEALPIX pixelisation of the sphere [62], where planar ridgelet and curvelet transforms are performed on each of the twelve base-resolution faces of the HEALPIX pixelisation.

Such an approach does not lead to ridgelets and curvelets that live natively on the sphere. The corresponding ridgelet transform does not probe signal content along great circles on the sphere, as one would expect, and the curvelet transform may result in blocking artefacts, as acknowledged in [30] (the twelve base-resolution faces of the HEALPIX pixelisation are treated independently and there is no overlapping of blocks that belong to different base-resolution pixels). When analysing data on the sphere, it is suggested that multiple rotated versions of the data could be analysed to mitigate these blocking artefacts [30]. Second-generation curvelets on the sphere have been constructed recently in [63], which live natively on the sphere, exhibit the parabolic scaling relation typical of curvelets, and do not suffer any blocking artefacts.

An alternative ridgelet transform on the sphere has been constructed in [64]. This construction lives natively on the sphere, probes signal content along great circles and does not exhibit any blocking artefacts. These properties are essential for the analysis of diffusion MRI signals, which motivates the construction. The ridgelet transform is constructed from a standard spherical Radon transform, followed by a wavelet transform on the sphere. Although this construction has many desirable properties and has already been demonstrated to be of considerable practical use [64], [65], it has two shortcomings. Firstly, it depends on an *ad hoc* scaling parameter. For the practical setting where the order of the transform must be fixed, some choices of the scaling parameter will perform better than others, as the authors acknowledge [64]. Secondly, the forward ridgelet transform does not afford an explicit inverse transform. Instead, inversion is performed in an iterative manner by an orthogonal matching pursuit algorithm [64].

In this article, we develop a ridgelet transform on the sphere that exhibits all of the desirable properties of the construction of [64], namely: it lives natively on the sphere, probes signal content along great circles and does not exhibit any blocking artefacts. Moreover, our construction does not depend on an *ad hoc* scaling parameter and exhibits an explicit inverse transform that can be computed efficiently and exactly for signals exhibiting antipodal symmetry. Our ridgelet transform on the sphere is built on a novel view of the spherical Radon transform as a convolution, and its resulting harmonic representation, and on the scale-discretised wavelet transform on the sphere [25]–[27], [35], [44]. Furthermore, we extend the spherical Radon and ridgelet transforms to the analysis of spin signals on the sphere.

The remainder of this article is structured as follows. Harmonic analysis on the sphere is review concisely in Sec. II. We present a novel take on the spherical Radon transform in Sec. III, viewing it as a convolution on the sphere, which leads to a straightforward derivation of its harmonic action. The scale-discretised wavelet transform on the sphere is discussed in Sec. IV, which is combined with the spherical Radon transform to construct a spherical ridgelet transform in Sec. V. The numerical implementation of our ridgelet transform is presented and evaluated in Sec. VI and an illustrative application to diffusion MRI is presented in Sec. VII. Concluding remarks are made in Sec. VIII.

II. Harmonic Analysis on the Sphere

We concisely review harmonic analysis on the sphere in this section, presenting the mathematical preliminaries required throughout the remainder of the article. Scalar and spin signals on the sphere are first reviewed and our notation established, before we describe the spherical harmonic decompositions of such functions. We then describe the rotation of functions on the sphere, followed by a review of convolution on the sphere with axisymmetric kernels, expressed in both the spatial and harmonic domains.

A. Scalar and spin signals

We consider the space of square integrable functions on the sphere $\mathrm{L}^2(\mathbb{S}^2)$, with the inner product of $f, g \in \mathrm{L}^2(\mathbb{S}^2)$ defined by

$$\langle f,\, g\rangle \equiv \int_{\mathbb{S}^2} \mathrm{d}\Omega(\theta,\varphi)\, f(\theta,\varphi)\, g^*(\theta,\varphi)\,,$$

where $\mathrm{d}\Omega(\theta,\varphi) = \sin\theta\,\mathrm{d}\theta\,\mathrm{d}\varphi$ is the usual invariant measure on the sphere and (θ,φ) define spherical coordinates with colatitude $\theta \in [0,\pi]$ and longitude $\varphi \in [0,2\pi)$. Complex conjugation is denoted by the superscript *.

All of the transforms presented in this article are formulated for the analysis of both scalar and spin signals on the sphere. Although the scalar setting dominates practical applications of these transforms, we nevertheless present the general spin setting, which specialises to the scalar setting simply by setting the spin number $s \in \mathbb{Z}$ to zero. The reader more interested in practical applications of the analysis of scalar signals on the sphere may simply ignore the spin generalisation and consider $s = 0$ throughout.

Square integrable spin functions on the sphere ${}_sf \in \mathrm{L}^2(\mathbb{S}^2)$, with integer spin $s \in \mathbb{Z}$, are defined by their behaviour under local rotations. By definition, a spin function transforms as [38], [66], [67]

$${}_sf'(\theta,\varphi) = \exp(-\mathrm{i}s\chi)\; {}_sf(\theta,\varphi) \tag{1}$$

under a local rotation by $\chi \in [0,2\pi)$, where the prime denotes the rotated function.[1] It is important to note that the rotation considered here is *not* a global rotation on the sphere but rather a rotation by χ in the tangent plane centred on the spherical coordinates (θ,φ).

B. Spherical harmonic representations

The spin spherical harmonics ${}_sY_{\ell m} \in \mathrm{L}^2(\mathbb{S}^2)$ form an orthogonal basis for $\mathrm{L}^2(\mathbb{S}^2)$ spin s functions on the sphere, for natural $\ell \in \mathbb{N}$ and integer $m \in \mathbb{Z}$, $|m| \leq \ell$, $|s| \leq \ell$. The orthogonality and completeness relations for the spherical harmonics read $\langle {}_sY_{\ell m},\, {}_sY_{\ell' m'}\rangle = \delta_{\ell\ell'}\delta_{mm'}$ and

$$\sum_{\ell=0}^{\infty}\sum_{m=-\ell}^{\ell} {}_sY_{\ell m}(\theta,\varphi)\, {}_sY^*_{\ell m}(\theta',\varphi') = \delta(\cos\theta - \cos\theta')\delta(\varphi-\varphi') \tag{2}$$

[1] The sign convention adopted for the argument of the complex exponential differs to the original definition [66] but is identical to the convention used in the context of the polarisation of the CMB [38].

respectively [38], [66], [67], where δ_{ij} is the Kronecker delta symbol and $\delta(\cdot)$ is the one-dimensional Dirac delta function.

The spin spherical harmonics may be defined by the Wigner functions $D^{\ell}_{mn}(\alpha, \beta, \gamma)$ through [67]

$$ {}_sY_{\ell m}(\theta, \varphi) = (-1)^s \sqrt{\frac{2\ell+1}{4\pi}}\, D^{\ell\,*}_{m,-s}(\varphi, \theta, 0) \,, \tag{3}$$

where the Wigner functions $D^{\ell}_{mn}(\alpha, \beta, \gamma)$, for natural $\ell \in \mathbb{N}$ and integer $m, n \in \mathbb{Z}$, form an orthogonal basis for the space $\mathrm{L}^2(\mathrm{SO}(3))$ of square integrable functions on the rotation group, and are parameterised by the Euler angles (α, β, γ), where $\alpha \in [0, 2\pi)$, $\beta \in [0, \pi]$ and $\gamma \in [0, 2\pi)$.[2] The Wigner functions may be decomposed as [68]

$$ D^{\ell}_{mn}(\alpha, \beta, \gamma) = \mathrm{e}^{-\mathrm{i}m\alpha}\, d^{\ell}_{mn}(\beta)\, \mathrm{e}^{-\mathrm{i}n\gamma} \,, \tag{4}$$

where the real polar d-functions are defined in, *e.g.*, [68]. Consequently, the spin spherical harmonics may be written as

$$ {}_sY_{\ell m}(\theta, \varphi) = (-1)^s \sqrt{\frac{2\ell+1}{4\pi}}\, d^{\ell}_{m,-s}(\theta)\, \mathrm{e}^{\mathrm{i}n\varphi} \,. \tag{5}$$

In the scalar setting $s = 0$, Eq. (5) reduces to the familiar form

$$ Y_{\ell m}(\theta, \varphi) = \sqrt{\frac{2\ell+1}{4\pi}\frac{(\ell-m)!}{(\ell+m)!}}\, P^m_{\ell}(\cos\theta)\, \exp(\mathrm{i}m\varphi) \,, \tag{6}$$

where $P^m_{\ell}(\cdot)$ are the associated Legendre functions. We adopt the Condon-Shortley phase convention, with the $(-1)^m$ phase factor included in the definition of the associated Legendre functions, ensuring the conjugate symmetry relation ${}_sY^*_{\ell m}(\theta, \varphi) = (-1)^{s+m}\, {}_{-s}Y_{\ell,-m}(\theta, \varphi)$ holds.

Due to the orthogonality and completeness of the spin spherical harmonics, any square integrable spin function on the sphere ${}_sf \in \mathrm{L}^2(\mathbb{S}^2)$ may be represented by its spherical harmonic expansion

$$ {}_sf(\theta, \varphi) = \sum_{\ell=0}^{\infty} \sum_{m=-\ell}^{\ell} {}_sf_{\ell m}\, {}_sY_{\ell m}(\theta, \varphi) \,, \tag{7}$$

where the spin spherical harmonic coefficients are given by the usual projection onto each basis function:

$$ {}_sf_{\ell m} = \langle {}_sf,\, {}_sY_{\ell m} \rangle \,. \tag{8}$$

The spin spherical harmonic coefficients of a signal satisfying ${}_sf^* = {}_{-s}f$ (which for a spin $s = 0$ function equates to the usual reality condition), satisfy the conjugate symmetry relation

$$ {}_sf^*_{\ell m} = (-1)^{s+m}\, {}_{-s}f_{\ell,-m} \,, \tag{9}$$

which follows directly from the conjugate symmetry of the spin spherical harmonics.

Throughout, we consider signals on the sphere band-limited at L, that is signals such that ${}_sf_{\ell m} = 0, \forall \ell \geq L$. The spherical harmonic transform of Eq. (8) can be computed exactly and efficiently for band-limited signals by appealing to sampling theorems on the sphere and fast algorithms [69]–[75].

[2]We adopt the zyz Euler convention corresponding to the rotation of a physical body in a *fixed* co-ordinate system about the z, y and z axes by γ, β and α respectively.

C. Rotation of signals

The rotation of a function on the sphere may be performed by application of the rotation operator $\mathcal{R}_{(\alpha,\beta,\gamma)}$, characterised by elements of the rotation group $\mathrm{SO}(3)$, parameterised by the Euler angles (α, β, γ). The action of the rotation operator $\mathcal{R}_{(\alpha,\beta,\gamma)}$ on a function on the sphere is defined by

$$ \big(\mathcal{R}_{(\alpha,\beta,\gamma)}\, {}_sf\big)(\theta, \varphi) \equiv {}_sf\big(\mathsf{R}^{-1}_{(\alpha,\beta,\gamma)}\hat{\boldsymbol{\omega}}\big) \,, \tag{10}$$

where $\mathsf{R}_{(\alpha,\beta,\gamma)}$ is the three-dimensional rotation matrix corresponding to $\mathcal{R}_{(\alpha,\beta,\gamma)}$ and $\hat{\boldsymbol{\omega}}$ denotes the Cartesian vector corresponding to (θ, φ).

Since we subsequently consider axisymmetric convolution, we will be concerned with the rotation of axisymmetric kernel functions ${}_sh \in \mathrm{L}^2(\mathbb{S}^2)$ on the sphere, *i.e.* kernels that are invariant under azimuthal rotation when centred on the North pole: $\mathcal{R}_{(0,0,\gamma)}\, {}_sh = {}_sh$. Consequently, we adopt the shorthand notation $\mathcal{R}_{(\beta,\alpha)} \equiv \mathcal{R}_{(\alpha,\beta,0)}$.

D. Axisymmetric convolution

Convolution on the sphere can be defined in a variety of manners [69], [74]–[78]. We consider the axisymmetric convolution operator, denoted $\odot$, where the convolution of a function ${}_sf \in \mathrm{L}^2(\mathbb{S}^2)$ with an axisymmetric kernel ${}_sh \in \mathrm{L}^2(\mathbb{S}^2)$ is defined by

$$\begin{aligned} ({}_sf \odot {}_sh)(\theta, \varphi) &\equiv \langle {}_sf,\, \mathcal{R}_{(\theta,\varphi)}\, {}_sh \rangle \\ &= \int_{\mathbb{S}^2} \mathrm{d}\Omega(\theta', \varphi')\, f(\theta', \varphi')\, \big(\mathcal{R}_{(\theta,\varphi)}\, {}_sh\big)^*(\theta', \varphi') \,. \end{aligned} \tag{11}$$

Although the convolution of Eq. (11) can be generalised to a directional convolution in a straightforward manner [74], [75] (by adopting a directional kernel and considering all rotations over $\mathrm{SO}(3)$) we do not require such a generalisation here.

Axisymmetric convolution may be expressed by its harmonic expansion:

$$ ({}_sf \odot {}_sh)(\theta, \varphi) = \sum_{\ell=0}^{\infty} \sum_{m=-\ell}^{\ell} \sqrt{\frac{4\pi}{2\ell+1}}\, {}_sf_{\ell m}\, {}_sh^*_{\ell 0}\, Y_{\ell m}(\theta, \varphi) \,, \tag{12}$$

where the spin spherical harmonic coefficients of ${}_sf$ and ${}_sh$ are given by ${}_sf_{\ell m} = \langle {}_sf,\, {}_sY_{\ell m} \rangle$ and ${}_sh_{\ell 0}\delta_{m0} = \langle {}_sh,\, {}_sY_{\ell m} \rangle$, respectively, where the azimuthal symmetry of ${}_sh$ implies its harmonic coefficients are non-zero for $m = 0$ only. Although Eq. (12) is well-known, we present a derivation in Appendix A for completeness. Notice that although two spin functions are convolved, the resultant $({}_sf \odot {}_sh)$ is a scalar ($s = 0$) function on the sphere.

III. Spherical Radon Transform

We present a novel take on the well-known spherical Radon transform, viewing it as an axisymmetric convolution, which leads to a straightforward derivation of its harmonic action. This harmonic representation motivates an inverse transform for antipodal signals, which is well-behaved up to very high harmonic degrees ℓ. We conclude this section by noting some properties of the spherical Radon transform.

A. Forward transform

The spherical Radon transform, also known as the Funk-Radon transform, is given by [51]

$$(\mathcal{S}_s f)(\theta,\varphi) \equiv \int_{\mathbb{S}^2} \mathrm{d}\Omega(\theta',\varphi')\; {}_s f(\theta',\varphi')\, \delta(\hat{\boldsymbol{\omega}}' \cdot \hat{\boldsymbol{\omega}})\,, \quad (13)$$

where $\hat{\boldsymbol{\omega}}$ and $\hat{\boldsymbol{\omega}}'$ denote the Cartesian corresponding to angular coordinates $\omega = (\theta,\varphi)$ and $\omega' = (\theta',\varphi')$, respectively, and $\delta(\cdot)$ is again the one-dimensional Dirac delta. In words, the spherical Radon transform is the collection of line integrals of ${}_s f$ along great circles with poles at $\omega = (\theta,\varphi)$, projected onto the point defined by the poles of the great circles.

By defining the Funk-Radon kernel $\xi(\theta,\varphi) \equiv \delta(\theta - \pi/2)$, the spherical Radon transform may be expressed as an axisymmetric convolution by

$$\begin{aligned}(\mathcal{S}_s f)(\theta,\varphi) &= \int_{\mathbb{S}^2} \mathrm{d}\Omega(\theta',\varphi')\; {}_s f(\theta',\varphi')\, (\mathcal{R}_{(\theta,\varphi)}\xi)(\theta',\varphi') \\ &= ({}_s f \odot \xi)(\theta,\varphi)\,. \end{aligned} \quad (14)$$

Consequently, by noting Eq. (12), the spherical Radon transform can be expressed in harmonic space by

$$(\mathcal{S}_s f)_{\ell m} = ({}_s f \odot \xi)_{\ell m} = \sqrt{\frac{4\pi}{2\ell+1}}\; {}_s f_{\ell m}\; {}_s\xi^*_{\ell 0}\,, \quad (15)$$

where the spin harmonic coefficients of the Funk-Radon kernel ${}_s\xi_{\ell m} = \langle \xi,\, {}_sY_{\ell m}\rangle$ are given by

$${}_s\xi_{\ell m} = (-1)^s \sqrt{\pi(2\ell+1)}\, \sqrt{\frac{(\ell-s)!}{(\ell+s)!}}\, P_\ell^s(0)\, \delta_{m0}\,, \quad (16)$$

as shown in Appendix B. The harmonic representation of the spherical Radon transform then becomes

$$(\mathcal{S}_s f)_{\ell m} = 2\pi\,(-1)^s \sqrt{\frac{(\ell-s)!}{(\ell+s)!}}\, P_\ell^s(0)\; {}_s f_{\ell m}\,, \quad (17)$$

Note that for the scalar case ($s = 0$), Eq. (17) reduces to the expressions derived in [53]–[55], however each of these results are recovered following alternative derivations. Viewing the spherical Radon transform as an axisymmetric convolution helps to aid intuition and, consequently, the derivation of Eq. (17) follows in a straightforward manner.

B. Inverse transform

From the harmonic representation of the spherical Radon transform given by Eq. (17), it is clear that the transform can be inverted if the associated Legendre functions are well-behaved at the origin. We derive an explicit expression for $P_\ell^s(0)$ in Appendix C and show that $P_\ell^s(0) = \mathcal{O}(\ell^{-1/2})$ as $\ell \to \infty$, for $s \ll \ell$ (which is typically the case in practice) and for $\ell + s$ even, while for $\ell + s$ odd, $P_\ell^s(0) = 0$. Consequently, the spherical Radon transform of signals with non-zero harmonic coefficients for $\ell + s$ even only, can be inverted by

$${}_s f_{\ell m} = (\mathcal{S}^{-1}\mathcal{S}_s f)_{\ell m} \equiv \frac{(\mathcal{S}_s f)_{\ell m}}{2\pi\,(-1)^s \sqrt{\frac{(\ell-s)!}{(\ell+s)!}}\, P_\ell^s(0)}\,. \quad (18)$$

In practice, inversion can be performed accurately up to very high ℓ.

For scalar signals, the restriction to signals with harmonic coefficients non-zero for even ℓ only corresponds to signals with antipodal symmetry (*i.e.* signals that are invariant under the transformation $\hat{\boldsymbol{\omega}} \to -\hat{\boldsymbol{\omega}}$). Such a condition is expected since the signal on the sphere recovered from the forward spherical Radon transform is itself antipodal.

C. Properties

We conclude our discussion of the spherical Radon transform by noting two important properties.

1) Shift invariance: The spherical Radon transform is shift invariant, such that

$$\big(\mathcal{S}\,\mathcal{R}_{(\alpha,\beta,\gamma)}\; {}_s f\big)(\theta,\varphi) = \big(\mathcal{R}_{(\alpha,\beta,\gamma)}\,\mathcal{S}\; {}_s f\big)(\theta,\varphi)\,. \quad (19)$$

This property can be shown by noting the harmonic representation of the spherical Radon transform and the rotation of the spin spherical harmonics given by Eq. (43).

2) Eigenfunctions and eigenvalues: By considering the spherical Radon transform of the spin spherical harmonics ${}_sY_{\ell m}$, we see from Eq. (17) that

$$(\mathcal{S}_s Y_{\ell m})(\theta,\varphi) = {}_s\lambda_\ell\; {}_sY_{\ell m}(\theta,\varphi)\,, \quad (20)$$

where

$${}_s\lambda_\ell = 2\pi\,(-1)^s \sqrt{\frac{(\ell-s)!}{(\ell+s)!}}\, P_\ell^s(0)\,. \quad (21)$$

The spin spherical harmonics are therefore the eigenfunctions of the spherical Radon transform, with corresponding eigenvalues ${}_s\lambda_\ell$.

IV. Spherical Wavelet Transform

In the ridgelet construction that follows in Sec. V we adopt the scale-discretised wavelet transform on the sphere, which is reviewed concisely in this section. Although scale-discretised wavelets are typically directional, we specialise to the axisymmetric setting (simply by setting the azimuthal band-limit of scale-discretised wavelets to $N = 1$). For further details we refer the reader to [25]–[27], [35], [44].

A. Wavelet analysis

The scale-discretised wavelet transform on the sphere, when restricted to axisymmetric wavelets ${}_s\Psi^{(j)} \in \mathrm{L}^2(\mathbb{S}^2)$, is defined by the axisymmetric convolution

$$W^{{}_s\Psi^{(j)}}(\theta,\varphi) \equiv (\mathcal{W}^{{}_s\Psi^{(j)}}\; {}_s f)(\theta,\varphi) \equiv ({}_s f \odot {}_s\Psi^{(j)})(\theta,\varphi)\,, \quad (22)$$

with wavelet coefficients $W^{{}_s\Psi^{(j)}} \in \mathrm{L}^2(\mathbb{S}^2)$ defined on the sphere and where $\mathcal{W}^{{}_s\Psi^{(j)}}$ denotes the wavelet transform operator. The wavelets are designed to be localised in both scale and position, hence the wavelet coefficients probe signal content localised simultaneously in scale and space. The wavelet scale $j \in \mathbb{N}_0$ encodes the angular localisation of $\Psi^{(j)}$. The wavelets do not probe the low-frequency content of the signal; hence, a

scaling function ${}_s\Phi^{(j)} \in \mathrm{L}^2(\mathbb{S}^2)$ is introduced for this purpose, with scaling coefficients $W^{{}_s\Phi^{(j)}} \in \mathrm{L}^2(\mathbb{S}^2)$ given by

$$W^{{}_s\Phi}(\theta,\varphi) \equiv (\mathcal{W}^{{}_s\Phi}\,{}_sf)(\theta,\varphi) \equiv ({}_sf \odot {}_s\Psi)(\theta,\varphi)\,. \quad (23)$$

The explicit construction of the wavelets and scaling function is discussed in Sec. IV-C. We adopt the shorthand notation

$$W^{\{{}_s\Psi^{(j)},\,{}_s\Phi\}_j}(\theta,\varphi) \equiv (\mathcal{W}^{\{{}_s\Psi^{(j)},\,{}_s\Phi\}_j}\,{}_sf)(\theta,\varphi)\,, \quad (24)$$

to denote the wavelet transform for all wavelets (indexed by j) and the scaling function, or simply

$$\boldsymbol{W}(\theta,\varphi) \equiv ({}_s\boldsymbol{\mathcal{W}}\,{}_sf)(\theta,\varphi)\,. \quad (25)$$

Bold notation is used to highlight that we recover a collection (*cf.* vector) of wavelet (and scaling) coefficients. Finally, note that the wavelet and scaling coefficients of spin functions are scalar functions on the sphere.

B. Wavelet synthesis

The signal ${}_sf$ can be synthesised exactly from its wavelet and scaling coefficients by

$$\begin{aligned}{}_sf(\theta,\varphi) = &\int_{\mathbb{S}^2} \mathrm{d}\Omega(\theta',\varphi')\, W_s\Phi(\theta',\varphi')\, (\mathcal{R}_{(\theta',\varphi')}\,{}_s\Phi)(\theta,\varphi)\\ &+ \sum_{j=J_0}^{J} \int_{\mathbb{S}^2} \mathrm{d}\Omega(\theta',\varphi')\, W^{{}_s\Psi^j}(\theta',\varphi')\, (\mathcal{R}_{(\theta',\varphi')}\,{}_s\Psi^{(j)})(\theta,\varphi)\,,\end{aligned} \quad (26)$$

where J_0 and J are the minimum and maximum wavelet scales considered, respectively, *i.e.* $0 \leq J_0 \leq j \leq J$. We adopt the j indexing convention of [26], [35], whence the minimum and maximum permissible wavelet scales are defined for the analysis of band-limited signals. We adopt the shorthand notation

$${}_sf(\theta,\varphi) = ({}_s\boldsymbol{\mathcal{W}}^{-1}\boldsymbol{W})(\theta,\varphi) \quad (27)$$

to denote wavelet synthesis, which is the notational analogue of Eq. (25). To ensure perfect synthesis the wavelets and scaling function must satisfy an admissibility condition given by the following resolution of the identity:

$$\frac{4\pi}{2\ell+1}|\Phi_{\ell 0}|^2 + \frac{4\pi}{2\ell+1}\sum_{j=J_0}^{J}|\Psi^{(j)}_{\ell 0}|^2 = 1\,, \quad \forall \ell\,, \quad (28)$$

where $\Phi_{\ell 0}\delta_{m0} = \langle \Phi,\, Y_{\ell m}\rangle$ and $\Psi^{(j)}_{\ell 0}\delta_{m0} = \langle \Psi^{(j)},\, Y_{\ell m}\rangle$ are the spherical harmonic coefficients of Φ and $\Psi^{(j)}$.

In practice, for band-limited functions, wavelet analysis and synthesis can be computed: (i) exactly (to machine precision), since one may appeal to sampling theorems and corresponding exact quadrature rules for the computation of integrals [72], [73]; and (ii) efficiently, by developing fast algorithms [26], [27], [35], [74], which scale to very large data-sets containing tens of millions of samples on the sphere. An implementation of the scale-discretised wavelet transform on the sphere is publicly available in the S2LET[3] code.

[3] http://www.s2let.org

C. Wavelet construction

Consider a smoothly decreasing function $k_\lambda(t)$ which is unity for $t < \lambda^{-1}$, zero for $t > 1$, and is smoothly decreasing from unity to zero for $t \in [\lambda^{-1}, 1]$ (defined explicitly in [25]–[27], [35], [44]). Define the wavelet kernel generating function by

$$\kappa_\lambda(t) \equiv \sqrt{k_\lambda(\lambda^{-1}t) - k_\lambda(t)}\,, \quad (29)$$

which has compact support $t \in [\lambda^{-1}, \lambda]$ and reaches a peak of unity at $t = 1$. The scale-discretised wavelet kernel for scale j is then defined by

$$\kappa^{(j)}(\ell) \equiv \kappa_\lambda(\lambda^{-j}\ell)\,, \quad (30)$$

which has compact support on $\ell \in \big[\lfloor\lambda^{j-1}\rfloor, \lceil\lambda^{j+1}\rceil\big]$, where $\lfloor\cdot\rfloor$ and $\lceil\cdot\rceil$ are the floor and ceiling functions, respectively. Finally, define the the wavelets in harmonic space by

$${}_s\Psi_{\ell m} \equiv \sqrt{\frac{2\ell+1}{4\pi}}\,\kappa^{(j)}(\ell)\,\delta_{m0}\,, \quad (31)$$

and the scaling function by

$${}_s\Phi_{\ell m} \equiv \sqrt{\frac{2\ell+1}{4\pi}}\,\sqrt{k_\lambda(\lambda^{-J_0}\ell)}\,\delta_{m0}\,. \quad (32)$$

By such a construction, the wavelets and scaling functions tile the harmonic line ℓ, while satisfying the admissibility condition of Eq. (28). The parameter J_0 is chosen so that the scaling function captures frequency content for $\ell < \lambda^{J_0}$ (for the case $J_0 = 0$, the scaling function captures $\ell = 0$ only, *i.e.* the mean of the signal analysed). The wavelet at scale j has harmonic support within $\ell \in \big[\lfloor\lambda^{j-1}\rfloor, \lceil\lambda^{j+1}\rceil\big]$, while also being smooth. Consequently, the wavelets are well-localised in both the spatial and harmonic domains. It is shown in [44] that scale-discretised wavelets exhibit excellent concentration properties.

V. Spherical Ridgelet Transform

We present a novel spherical ridgelet transform on the sphere by composing the spherical Radon transform and the scale-discretised wavelet transform. Our construction permits an explicit inverse transform to synthesise antipodal signals from their ridgelet coefficients exactly and satisfies a number of additional desirable properties that are lacking in alternative constructions.

A. Ridgelet analysis

We define the ridgelet transform on the sphere by the axisymmetric convolution with the ridgelet ${}_s\psi^{(j)} \in \mathrm{L}^2(\mathbb{S}^2)$:

$$\begin{aligned}G^{{}_s\psi^{(j)}}(\theta,\varphi) &\equiv (\mathcal{G}^{{}_s\psi^{(j)}}\,{}_sf)(\theta,\varphi) \equiv ({}_sf \odot {}_s\psi^{(j)})(\theta,\varphi)\\ &= \int_{\mathbb{S}^2} \mathrm{d}\Omega(\theta',\varphi')\; {}_sf(\theta',\varphi')\; (\mathcal{R}_{(\theta,\varphi)}\,{}_s\psi^{(j)})(\theta',\varphi')\,,\end{aligned} \quad (33)$$

with ridgelet coefficients $G^{{}_s\psi^{(j)}} \in \mathrm{L}^2(\mathbb{S}^2)$ defined on the sphere and where $\mathcal{G}^{{}_s\Psi^{(j)}}$ denotes the ridgelet transform operator.

The rotated ridgelet $\mathcal{R}_{(\theta,\varphi)}\,{}_s\psi^{(j)}(\theta',\varphi')$ should be constant along the great circle defined by $\hat{\boldsymbol{\omega}}\cdot\hat{\boldsymbol{\omega}}' = 0$ and a wavelet transverse to the ridge defined by the great circle. Recall that

$\hat{\boldsymbol{\omega}}$ and $\hat{\boldsymbol{\omega}}'$ denote the Cartesian coordinates corresponding to angular coordinates $\omega = (\theta, \varphi)$ and $\omega' = (\theta', \varphi')$, respectively. Such a ridgelet on the sphere can be constructed from an axisymmetric convolution of the Funk-Radon kernel ξ with the axisymmetric wavelet ${}_0\Psi^{(j)}$:

$$ {}_s\psi^{(j)}(\theta, \varphi) \equiv (\xi \odot {}_0\Psi^{(j)})(\theta, \varphi) \,. \tag{34}$$

In Fig. 1 ridgelets are plotted for various scales j. Notice that the ridgelets exhibit precisely the structure desired (constant along ridges and wavelets transverse to ridges) and, analogous to Euclidean ridgelets, probe signal content along great circles (*cf.* global lines).

The ridgelet transform of Eq. (33) can then be viewed as the composition of a spherical Radon transform followed by a wavelet transform:

$$\begin{aligned} G^{{}_s\psi^{(j)}}(\theta, \varphi) &\equiv (\mathcal{G}^{{}_s\psi^{(j)}} {}_sf)(\theta, \varphi) \equiv ({}_sf \odot {}_s\psi^{(j)})(\theta, \varphi) \\ &= ({}_sf \odot \xi \odot {}_0\Psi^{(j)})(\theta, \varphi) \,, \end{aligned} \tag{35}$$

or in terms of operators

$$ \mathcal{G}^{{}_s\psi^{(j)}} = \mathcal{W}^{{}_0\Psi^{(j)}} \mathcal{S} \,. \tag{36}$$

Note that the ridget is constructed from scalar wavelets, since the axisymmetric convolution $({}_sf \odot \xi)$ is a scalar function on the sphere, even for spin signals ${}_sf$. A ridgelet scaling function ${}_s\phi^{(j)} \in \mathrm{L}^2(\mathbb{S}^2)$ must be defined to again capture the low-frequency content of the signal analysed. The construction of the scaling function is entirely analogous to the ridgelet construction just presented, hence:

$$ {}_s\phi^{(j)}(\theta, \varphi) \equiv (\xi \odot {}_0\Phi^{(j)})(\theta, \varphi) \,, \tag{37}$$

and

$$ \mathcal{G}^{{}_s\phi^{(j)}} = \mathcal{W}^{{}_0\Phi^{(j)}} \mathcal{S} \,. \tag{38}$$

Adopting the shorthand notation introduced in Sec. IV, we write the ridgelet transform for all ridgelets and the ridgelet scaling function by

$$ \boldsymbol{G}(\theta, \varphi) \equiv (\boldsymbol{\mathcal{G}}\ {}_sf)(\theta, \varphi) = ({}_0\boldsymbol{\mathcal{W}}\,\boldsymbol{\mathcal{S}}\ {}_sf)(\theta, \varphi) \,. \tag{39}$$

B. Ridgelet synthesis

The ridgelet transform can be inverted exactly for signals for which both the spherical wavelet and Radon transform can be inverted. Since the inverse spherical Radon transform is restricted to signals with non-zero harmonic coefficients for $\ell + s$ even only, the spherical ridgelet transform exhibits the same restriction. For scalar signals, this corresponds to signals with antipodal symmetry. Such a restriction is expected, since the ridgelet coefficients on the sphere exhibit antipodal symmetry themselves.

The signal ${}_sf$ can then by synthesised exactly from its ridgelet coefficients simply by invertering the composition of the Radon and wavelet transforms that comprise the ridgelet transform:

$$ {}_sf(\theta, \varphi) = (\boldsymbol{\mathcal{S}}^{-1}\,{}_0\boldsymbol{\mathcal{W}}^{-1}\boldsymbol{G})(\theta, \varphi) \,. \tag{40}$$

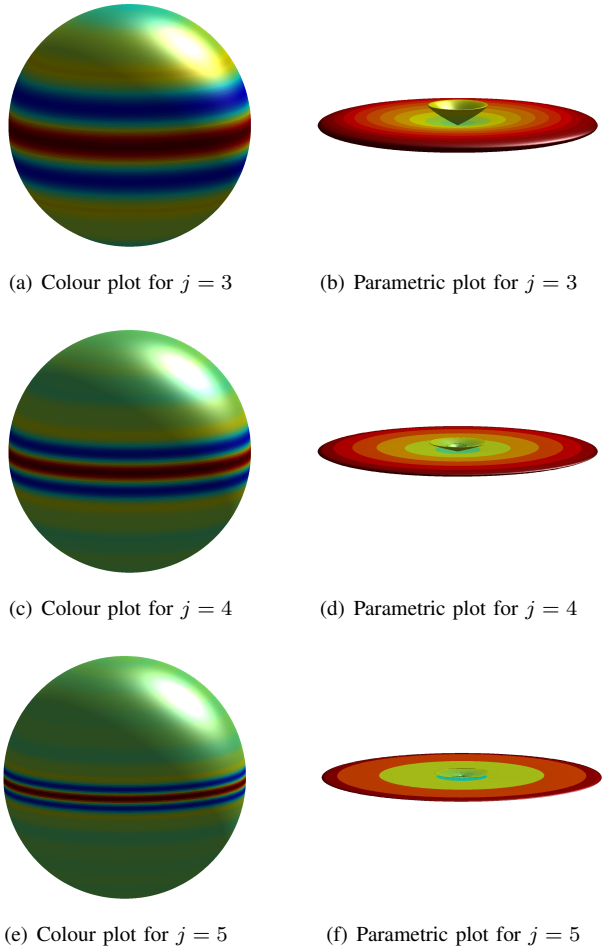

(a) Colour plot for $j = 3$ (b) Parametric plot for $j = 3$

(c) Colour plot for $j = 4$ (d) Parametric plot for $j = 4$

(e) Colour plot for $j = 5$ (f) Parametric plot for $j = 5$

Fig. 1. Spherical ridgelets, with axis aligned with the North pole, for various wavelet scales j, plotted on the sphere and parametrically. Notice that the constructed ridgelets are constant along ridges defined by great circles and wavelets transverse to ridges.

C. Properties

Analogous to Euclidean ridgelets, the spherical ridgelet transform consists of a spherical Radon transform, mapping singularities along great circles to point singularities, followed by a wavelet transform. Our ridgelet transform lives natively on the sphere, probes signal content globally along great circles, and does not exhibit any blocking artefacts. Moreover, we avoid any *ad hoc* scaling parameter. Most importantly, our ridgelet transform admits an explicit inverse transform, avoiding the need for iterative inversion techniques. No other ridgelet construction on the sphere exhibits all of the desirable properties of our construction.

VI. Evaluation

We have implemented the spherical Radon and ridgelet transforms in the existing S2LET [26], [35] code that supports the exact and efficient computation of scale-discretised wavelet transforms on the sphere. Support for both scalar and spin signals is implemented. The core algorithms of S2LET are implemented in C, while Matlab, Python, IDL and JAVA interfaces are also provided. S2LET is publicly available[4], and

[4] http://www.s2let.org

relies on the SSHT[5] code [72] to compute spherical harmonic transforms and the FFTW[6] code to compute Fourier transforms. In this section we evaluate, on simulations of random antipodal signals on the sphere, the numerical accuracy, computation time and asymptotic scaling of the S2LET implementation of the ridgelet transform on the sphere,

A. Simulations

We simulate band-limited test signals on the sphere defined by uniformly random spherical harmonic coefficients ${}_sf_{\ell m}$ with real and imaginary parts distributed in the interval $[-1, 1]$. For $\ell + s$ odd we set harmonic coefficients to zero to satisfy the symmetry condition required for invertibility of the spherical Radon and ridgelet transforms, which for scalar signals corresponds to antipodal signals. We then compute an inverse spherical harmonic transform to recover a band-limited signal on the sphere. A forward spherical ridgelet transform is then performed, followed by an inverse transform to synthesise the original signal from its ridgelet coefficients. Ten simulated signals are considered for band-limits from $L = 32$ to $L = 512$, although the spherical ridgelet transform can be computed up to band-limits of at least $L = 4096$ (*cf.* [72]). All numerical experiments are performed on a 2011 Macbook Air, with a 1.8 GHz Intel Core i7 processor and 4 GB of RAM.

B. Numerical accuracy

Numerical accuracy of a round-trip spherical ridgelet transform is measured by the maximum absolute error between the spherical harmonic coefficients of the original test signal ${}_sf^{\mathrm{o}}_{\ell m}$ and the recomputed values ${}_sf^{\mathrm{r}}_{\ell m}$, *i.e.* $\epsilon = \max_{\ell,m} \left| {}_sf^{\mathrm{r}}_{\ell m} - {}_sf^{\mathrm{o}}_{\ell m} \right|$. Results of the numerical accuracy tests, averaged over ten random test signals, are plotted in Fig. 2(a). Although we plot results for scalar signals, the accuracy of ridgelet transforms of spin signals is identical. The numerical accuracy of the round-trip transform is close to machine precision and found empirically to scale as $\mathcal{O}(L^2)$, with a factor of $\mathcal{O}(L)$ coming form the inversion of the spherical Radon transform and a factor of $\mathcal{O}(L)$ coming from the inversion of the spherical wavelet transform, which in turn follows from the inversion of the spherical harmonic transform.

C. Computation time

Computation time is measured by the round-trip computation time taken to perform a forward and inverse spherical ridgelet transform. Results of the computation time tests, averaged over ten random test signals, are plotted in Fig. 2(b). Although we plot results for scalar signals, the computation time for ridgelet transforms of spin signals is identical since the spin number is simply a parameter of the transform (rather than applied through spin lowering/raising operators). The computational complexity of the ridgelet transform is dominated by the spherical harmonic transform, which scales theoretically as $\mathcal{O}(L^3)$. From Fig. 2(b) the complexity of the ridgelet transform is found empirically to scale as $\mathcal{O}(L^3)$, as expected.

[5] http://www.spinsht.org
[6] http://www.fftw.org

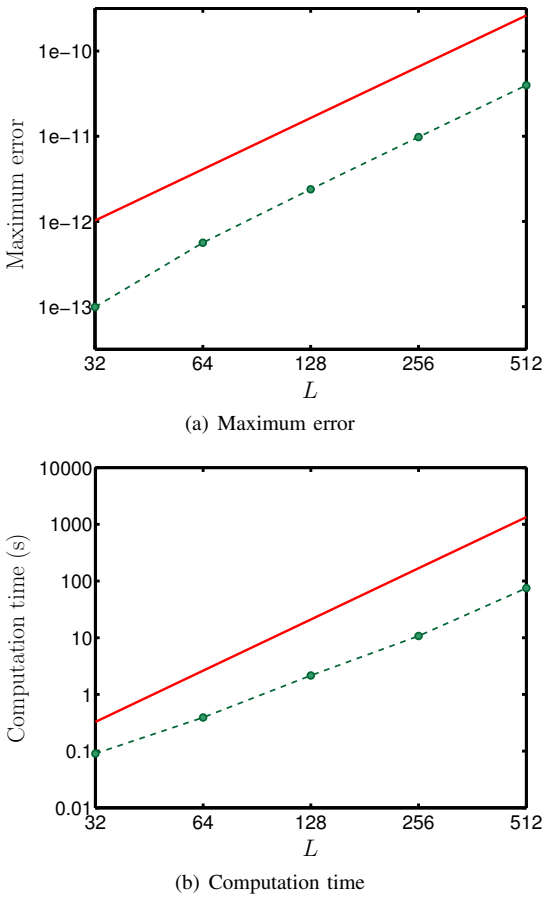

(a) Maximum error

(b) Computation time

Fig. 2. Numerical accuracy and computation time of the spherical ridgelet transform, averaged over ten round-trip transforms of random test signals. Numerical accuracy close to machine precision is achieved and found empirically to scale as $\mathcal{O}(L^2)$, with a factor of $\mathcal{O}(L)$ coming from the inversion of each of the spherical Radon and spherical wavelet transforms. Computation time is found empirically to scale as $\mathcal{O}(L^3)$, as expected theoretically. $\mathcal{O}(L^2)$ and $\mathcal{O}(L^3)$ scaling is shown by the solid red lines in panels (a) and (b) respectively.

VII. Illustration

In this section we illustrate the application of the spherical ridgelet transform to the analysis of diffusion MRI signals acquired on the sphere. The use of a spherical ridgelet transform to process diffusion MRI signals has been advocated already in [64], [65]. Here we present a simple illustration, simulating a diffusion MRI signal on the sphere and showing that its spherical ridgelet decomposition is sparse (formally, compressible), with few large ridgelet coefficients and many small coefficients.

A. Diffusion MRI signals on the sphere

Diffusion MRI can be used to study neuronal connections in the brain by measuring the diffusion of water molecules along white matter fibers. In so-called high angular resolution diffusion imaging (HARDI), diffusion MRI signals are sampled on spherical shells in each voxel of the brain. It has been shown that the probability distribution function

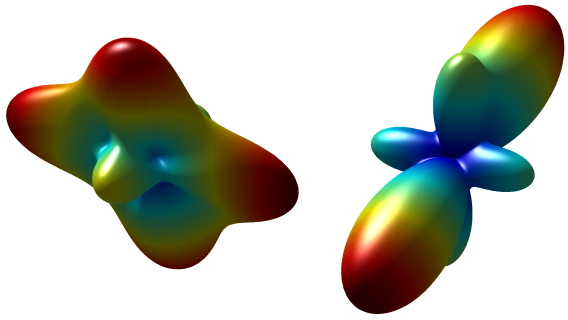

(a) HARDI signal (b) ODF signal

Fig. 3. Parametric plots of simulated diffusion MRI HARDI and ODF signals on the sphere, where the ODF is computed by the spherical Radon transform of the HARDI signal.

of fiber directions in each voxel, the so-called orientation distribution function (ODF), is approximately given by the spherical Radon transform of the HARDI signal acquired over a single spherical shell [52]. However, in practice acquired data is noisy and incomplete, motivating the development of a variety of ODF recovery techniques (for a review see [79]). Once the ODF is recovered in each voxel, global neural tracts in the brain are recovered though the process of tractography, which essentially involves piecing together the fiber directions embodied in the ODF of each voxel.

We simulate a HARDI signal over a spherical shell in a single voxel in order to examine its ridgelet decomposition in Sec. VII-B. The HARDI signal is modelled by a sum of weighted Gaussians, where each Gaussian corresponds to a different fiber passing through the voxel, and is given by (*e.g.* [64])

$$S(\hat{\boldsymbol{\omega}}) = \sum_i p_i \exp(-b\hat{\boldsymbol{\omega}}^{\mathrm{T}} \mathsf{D}_i \hat{\boldsymbol{\omega}}) \,, \qquad (41)$$

where D_i is the 3×3 diffusion tensor corresponding to fiber i, b is a constant dependent on the acquisition configuration, and p_i are weights associated with each fiber and sum to unity. We adopt the same parameters as the deterministic parameters adopted in the in silico experiments of [64], namely: $b = 3000$ s/mm^2 and $\mathsf{D} = \mathrm{diag}([1700, 300, 300])$ mm^2/s. Weights are uniformly randomly sampled in the interval $p_i \in [0.25, 0.75]$. Three fibers are considered, with D_i computed from D by random rotations aligned closely with the coordinate axes. The simulated HARDI signal and the corresponding ODF, computed by the spherical Radon transform of the HARDI signal, are plotted in Fig. 3. We simulate signals under ideal situations, in the absence of noise.

B. Diffusion MRI spherical ridgelet decomposition

Since the diffusion MRI HARDI signal is composed of a sum of contributions for each fibre that have their energy concentrated along great circles, it is suggested in [64], [65] that spherical ridgelets, which have their energy similarly distributed, are effective for representing HARDI signals and, in particular, more suitable than spherical harmonics. For the same reason, one would expect spherical ridgelets to be a more effective representation than spherical wavelets. We demonstrate and validate these predictions by examining a HARDI signal in both spherical wavelet and ridgelet representations.

In Fig. 4 we plot wavelet and ridgelet coefficients of the HARDI signal simulated in Sec. VII-A for a range of scales j. It is clear that ridgelet coefficients of the HARDI signal are sparser than wavelet coefficients, which exhibit many large peaks. For the ridgelet decompositions (Fig. 4, right column), the dominant directions of the ODF signal (Fig. 3(b)) are visible by eye, which is not the case for the wavelet decompositions (Fig. 4, left column). In Fig. 5 we plot histograms of wavelet and ridgelet coefficients for scale $j = 4$. It is again apparent that the ridgelet representation is sparser, with many coefficients close to zero and fewer large coefficients. The sparseness of HARDI signals in the spherical ridgelet decomposition, as demonstrated in this simple illustration, can be exploited in practical applications to handle noisy and incomplete data.

VIII. Conclusions

Although wavelet transforms on the sphere have proved very useful in many analyses of data acquired on spherical domains, they are not optimised to represent highly anisotropic signal content, such as lines or curvilinear structures. In Euclidean space, ridgelet and curvelet transforms have been devised for that purpose. Second-generation curvelets on the sphere have been constructed recently in [63].

In this article, we construct a ridgelet transform on the sphere that exhibits numerous desirable properties. Our ridgelet transform is defined natively on the sphere, probes signal content globally along great circles, does not exhibit blocking artefacts, does not rely of any *ad hoc* parameters and exhibits an explicit inverse transform. No alternative ridgelet construction on the sphere satisfies all of these properties.

Our ridgelet construction is built by composing the spherical Radon transform, also called the Funk-Radon transform, with the axisymmetric scale-discretised wavelet transform. We present a novel take on the spherical Radon transform, viewing it as a convolution with an axisymmetric kernel. Such a representation leads to a straightforward derivation of the harmonic action of the spherical Radon transform, which motives an exact inversion technique for signals that exhibit antipodal symmetry. Consequently, our spherical ridgelet transform also permits the exact inversion for antipodal signals. The restriction to antipodal signals is expected since the spherical Radon and ridgelet transforms themsleves result in signals that exhibit antipodal symmetry.

Our implementation of the spherical Radon and ridgelet transforms is made publicly available. Through simulations, we demonstrate that the numerical accuracy of our transforms is close to machine precision and can be applied to large data-sets supporting high band-limits L, with computational complexity scaling as $\mathcal{O}(L^3)$, as expected theoretically.

Finally, we illustrate the effectiveness of spherical ridgelets for imaging white matter fibers in the brain by diffusion MRI. We simulate a HARDI diffusion MRI signal on a single spherical shell and show that its spherical ridgelet coefficients

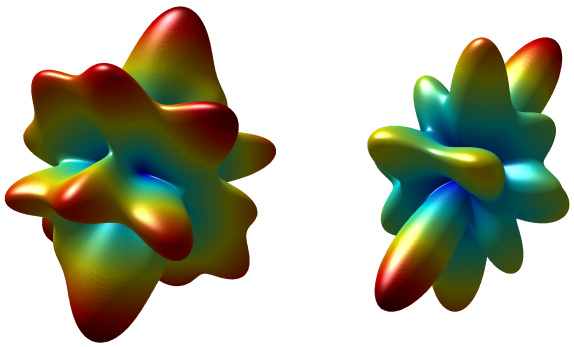

(a) Wavelet coefficients for $j = 3$ (b) Ridgelet coefficients for $j = 3$

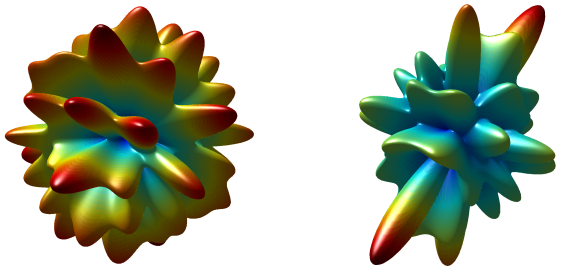

(c) Wavelet coefficients for $j = 4$ (d) Ridgelet coefficients for $j = 4$

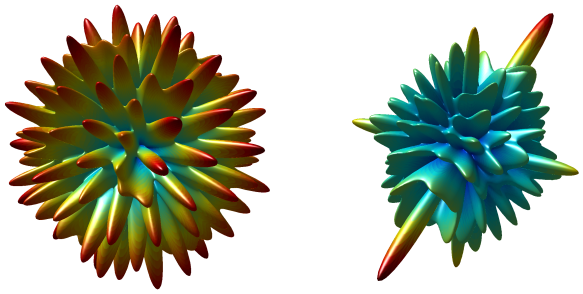

(e) Wavelet coefficients for $j = 5$ (f) Ridgelet coefficients for $j = 5$

Fig. 4. Parametric plots of spherical wavelet (left column) and ridgelet (right columns) coefficients of the HARDI signal plotted in Fig. 3(a). Notice that ridgelet coefficients are more sparse (*i.e.* fewer large coefficients) than the wavelet coefficients.

are much sparser that its spherical wavelet coefficients. The sparseness of HARDI signals in the spherical ridgelet decomposition can be exploited in practical applications to handle noisy and incomplete data.

In future work we intend to extend the spherical ridgelet transform presented here from the sphere to the 3D ball, *i.e.* the space formed by augmenting the sphere with the radial half-line (following the approach of the flaglet transform [40]). Such a transform would be particularly well-suited for the analysis of diffusion MRI signals in 3D, *i.e.* for aquisitions over mutliple concentric spherical shells. More generally, spherical ridgelets are also likely to be of practical use in many applications where signals exhibiting structure concentrated along great circles are encountered.

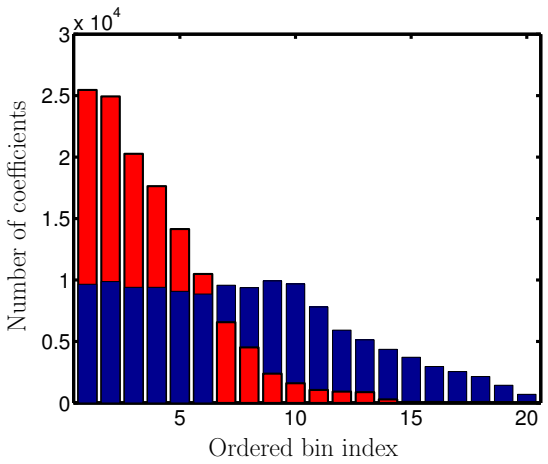

Fig. 5. Histogram of (the absolute value of) wavelet (blue) and ridgelet (red) coefficients for scale $j = 4$ of the HARDI signal plotted in Fig. 3(a). Notice that ridgelet coefficients are sparser than wavelet coefficients, with the ridgelet coefficients containing many coefficients close to zero and fewer large coefficients. The sparseness of the ridgelet coefficients of the HARDI signal demonstrates the suitability of spherical ridgelets for diffusion MRI.

Appendix A
Harmonic Representation of Axisymmetric Convolution

Substituting the harmonic decompositions of ${}_sf$ and ${}_sh$, the axisymmetric convolution of Eq. (11) reads

$$({}_sf \odot {}_sh)(\theta,\varphi) = \sum_{\ell=0}^{\infty} \sum_{m=-\ell}^{\ell} D^{\ell *}_{m0}(\varphi,\theta,0)\; {}_sf_{\ell m}\; {}_sh^*_{\ell 0}\;, \quad (42)$$

where we have noted the orthogonality of the spin spherical harmonics and that the spin spherical harmonics are rotated by [35]

$$\big(\mathcal{R}_{(\alpha,\beta,\gamma)}\, {}_sY_{\ell m}\big)(\theta,\varphi) = \sum_{n=-\ell}^{\ell} D^{\ell}_{nm}(\alpha,\beta,\gamma)\; {}_sY_{\ell n}(\theta,\varphi)\;. \quad (43)$$

The harmonic decomposition of Eq. (12) follows from Eq. (42) by Eq. (3).

Appendix B
Harmonic Representation of Funk-Radon Kernel

Computing the spin spherical harmonic coefficients of the Funk-Radon kernel we find

$$\begin{aligned} {}_s\xi_{\ell m} &= \langle \xi,\; {}_sY_{\ell m} \rangle \\ &= (-1)^s \sqrt{\pi(2\ell+1)}\; d^{\ell}_{m,-s}(\pi/2)\; \delta_{m0}\;, \end{aligned} \quad (44)$$

where we have noted the representation of spin spherical harmonics in terms of Wigner d-functions given by Eq. (5). Comparing Eq. (5) and Eq. (6) for the scalar setting where $s = 0$, it is apparent that the Wigner d-functions are related to the associated Legendre functions by

$$d^{\ell}_{m0}(\theta) = \sqrt{\frac{(\ell-m)!}{(\ell+m)!}}\; P^m_{\ell}(\cos\theta)\;. \quad (45)$$

By noting the symmetry relation [68]

$$d^{\ell}_{mn}(\theta) = d^{\ell}_{-n,-m}(\theta)\;, \quad (46)$$

the harmonic coefficients of the Funk-Radon kernel of Eq. (16) follow. Furthermore, the symmetry relation [68]

$$d^\ell_{mn}(\pi-\theta) = (-1)^{\ell+n} d^\ell_{-m,n}(\theta)\,, \tag{47}$$

implies $d^\ell_{0n}(\pi/2) = (-1)^{\ell+s} d^\ell_{0n}(\pi/2)$, which in turn implies ${}_s\xi_{\ell m} = 0$ for $\ell + s$ odd.

Appendix C
Associated Legendre Functions at the Origin

For argument $\theta = \pi/2$, the spherical harmonics become [68]

$$Y_{\ell m}(\pi/2,\varphi) = (-1)^{(\ell+m)/2} \exp(\mathrm{i}m\varphi) \times \sqrt{\frac{2\ell+1}{4\pi}\frac{(\ell+m-1)!!}{(\ell+m)!!}\frac{(\ell-m-1)!!}{(\ell-m)!!}}\,, \tag{48}$$

for $\ell + m$ even and zero otherwise. It follows that

$$P^m_\ell(0) = \frac{(-1)^{(\ell+m)/2}(\ell+m)!}{2^\ell \left(\frac{\ell+m}{2}\right)!\left(\frac{\ell-m}{2}\right)!}\,, \tag{49}$$

also for $\ell+m$ even and zero otherwise. Alternatively, Eq. (49) can be derived directly from the generating functions of the associated Legendre functions. In our implementation we compute $P^m_\ell(0)$ by Eq. (49), using the log-Gamma function to compute factorials to ensure numerical stability to high ℓ. By Stirling's approximation, the associated Legendre functions at the origin can be approximated by

$$P^m_\ell(0) \simeq \frac{(-1)^{(\ell+m)/2}\, 2^m \left(\frac{\ell+m}{2}\right)^{(\ell+m)/2}}{\sqrt{\pi(\ell-m)/2}\left(\frac{\ell-m}{2}\right)^{(\ell-m)/2}}\,. \tag{50}$$

It is apparent that $P^m_\ell(0) = \mathcal{O}(\ell^{-1/2})$ as $\ell \to \infty$, for $m \ll \ell$ (which is the case of interest in practice) and zero for $\ell + m$ even. Inverting the spherical Radon transform by Eq. (18) is thus well-conditioned up to very high degrees ℓ. For reference, $P^0_{4096}(0) \sim 10^{-2}$.

References

[1] P. Audet, "Directional wavelet analysis on the sphere: Application to gravity and topography of the terrestrial planets," *JGR*, vol. 116, no. E1, 2011.

[2] ——, "Toward mapping the effective elastic thickness of planetary lithospheres from a spherical wavelet analysis of gravity and topography," *Phys. Earth Planet In.*, vol. 226, no. 0, pp. 48–82, 2014.

[3] F. J. Simons, I. Loris, G. Nolet, I. C. Daubechies, S. Voronin, J. S. Judd, P. A. Vetter, J. Charléty, and C. Vonesch, "Solving or resolving global tomographic models with spherical wavelets, and the scale and sparsity of seismic heterogeneity," *GJI*, vol. 187, pp. 969–988, Nov. 2011.

[4] F. J. Simons, I. Loris, E. Brevdo, and I. C. Daubechies, "Wavelets and wavelet-like transforms on the sphere and their application to geophysical data inversion," in *SPIE Wavelets and Sparsity XIV*, 2011.

[5] P. Vielva, E. Martínez-González, R. B. Barreiro, J. L. Sanz, and L. Cayón, "Detection of non-Gaussianity in the WMAP 1-year data using spherical wavelets," *ApJ*, vol. 609, pp. 22–34, 2004.

[6] J. D. McEwen, M. P. Hobson, A. N. Lasenby, and D. J. Mortlock, "A high-significance detection of non-Gaussianity in the WMAP 1-year data using directional spherical wavelets," *MNRAS*, vol. 359, pp. 1583–1596, 2005.

[7] ——, "A high-significance detection of non-Gaussianity in the WMAP 3-year data using directional spherical wavelets," *MNRAS*, vol. 371, pp. L50–L54, 2006.

[8] ——, "A high-significance detection of non-Gaussianity in the WMAP 5-year data using directional spherical wavelets," *MNRAS*, vol. 388, no. 2, pp. 659–662, 2008.

[9] ——, "Non-Gaussianity detections in the Bianchi VII$_h$ corrected WMAP 1-year data made with directional spherical wavelets," *MNRAS*, vol. 369, pp. 1858–1868, 2006.

[10] P. Vielva, E. Martínez-González, and M. Tucci, "Cross-correlation of the cosmic microwave background and radio galaxies in real, harmonic and wavelet spaces: detection of the integrated Sachs-Wolfe effect and dark energy constraints," *MNRAS*, vol. 365, pp. 891–901, 2006.

[11] J. D. McEwen, P. Vielva, M. P. Hobson, E. Martínez-González, and A. N. Lasenby, "Detection of the ISW effect and corresponding dark energy constraints made with directional spherical wavelets," *MNRAS*, vol. 373, pp. 1211–1226, 2007.

[12] J. D. McEwen, Y. Wiaux, M. P. Hobson, P. Vandergheynst, and A. N. Lasenby, "Probing dark energy with steerable wavelets through correlation of WMAP and NVSS local morphological measures," *MNRAS*, vol. 384, no. 4, pp. 1289–1300, 2008.

[13] Planck Collaboration XII, "*Planck 2013* results. XII. Diffuse component separation," *A&A*, vol. 571, p. A12, 2014.

[14] Planck Collaboration XXIII, "*Planck* 2013 results. XXIII. Isotropy and statistics of the CMB," *A&A*, vol. 571, no. A23, 2014.

[15] Planck Collaboration XXV, "*Planck* 2013 results. XXV. Searches for cosmic strings and other topological defects," *A&A*, vol. 571, no. A25, 2014.

[16] J. D. McEwen, P. Vielva, Y. Wiaux., R. B. Barreiro, L. Cayón, M. P. Hobson, A. N. Lasenby, E. Martínez-González, and J. L. Sanz, "Cosmological applications of a wavelet analysis on the sphere," *JFAA*, vol. 13, no. 4, pp. 495–510, 2007.

[17] J.-P. Antoine and P. Vandergheynst, "Wavelets on the 2-sphere: a group theoretical approach," *ACHA*, vol. 7, pp. 1–30, 1999.

[18] ——, "Wavelets on the n-sphere and related manifolds," *J. Math. Phys.*, vol. 39, no. 8, pp. 3987–4008, 1998.

[19] Y. Wiaux, L. Jacques, and P. Vandergheynst, "Correspondence principle between spherical and Euclidean wavelets," *ApJ*, vol. 632, pp. 15–28, 2005.

[20] J. D. McEwen and A. M. M. Scaife, "Simulating full-sky interferometric observations," *MNRAS*, vol. 389, no. 3, pp. 1163–1178, 2008.

[21] J. D. McEwen, Y. Wiaux, and D. M. Eyers, "Data compression on the sphere," *A&A*, vol. 531, p. A98, 2011.

[22] F. J. Narcowich, P. Petrushev, and J. D. Ward, "Localized tight frames on spheres," *SIAM J. Math. Anal.*, vol. 38, no. 2, pp. 574–594, 2006.

[23] P. Baldi, G. Kerkyacharian, D. Marinucci, and D. Picard, "Asymptotics for spherical needlets," *Ann. Stat.*, vol. 37 No.3, pp. 1150–1171, 2009.

[24] D. Marinucci, D. Pietrobon, A. Balbi, P. Baldi, P. Cabella, G. Kerkyacharian, P. Natoli, D. Picard, and N. Vittorio, "Spherical needlets for cosmic microwave background data analysis," *MNRAS*, vol. 383, pp. 539–545, 2008.

[25] Y. Wiaux, J. D. McEwen, P. Vandergheynst, and O. Blanc, "Exact reconstruction with directional wavelets on the sphere," *MNRAS*, vol. 388, no. 2, pp. 770–788, 2008.

[26] B. Leistedt, J. D. McEwen, P. Vandergheynst, and Y. Wiaux, "S2LET: A code to perform fast wavelet analysis on the sphere," *A&A*, vol. 558, no. A128, pp. 1–9, 2013.

[27] J. D. McEwen, P. Vandergheynst, and Y. Wiaux, "On the computation of directional scale-discretized wavelet transforms on the sphere," in *SPIE Wavelets and Sparsity XV*, 2013.

[28] J. L. Sanz, D. Herranz, M. López-Caniego, and F. Argüeso, "Wavelets on the sphere – application to the detection problem," in *EUSIPCO*, Sept. 2006.

[29] J. D. McEwen, M. P. Hobson, and A. N. Lasenby, "A directional continuous wavelet transform on the sphere," *ArXiv*, 2006.

[30] J.-L. Starck, Y. Moudden, P. Abrial, and M. Nguyen, "Wavelets, ridgelets and curvelets on the sphere," *A&A*, vol. 446, pp. 1191–1204, Feb. 2006.

[31] D. Geller, F. K. Hansen, D. Marinucci, G. Kerkyacharian, and D. Picard, "Spin needlets for cosmic microwave background polarization data analysis," *PRD*, vol. 78, no. 12, pp. 123 533–+, 2008.

[32] D. Geller and D. Marinucci, "Spin Wavelets on the Sphere," *JFAA*, vol. 16, no. 6, pp. 840–884, Nov. 2010.

[33] ——, "Mixed Needlets," *J. Math. Anal. Appl.*, vol. 375, no. 2, pp. 610–630, June 2011.

[34] D. Geller, X. Lan, and D. Marinucci, "Spin Needlets Spectral Estimation," *Electron. J. Statist.*, vol. 3, pp. 1497–1530, July 2009.

[35] J. D. McEwen, B. Leistedt, M. Büttner, H. V. Peiris, and Y. Wiaux, "Directional spin wavelets on the sphere," *IEEE TSP, submitted*, 2015.

[36] J. D. McEwen, M. Büttner, B. Leistedt, H. V. Peiris, P. Vandergheynst, and Y. Wiaux, "On spin scale-discretised wavelets on the sphere for the analysis of CMB polarisation," in *Proceedings IAU Symposium No. 306, 2014*, 2014.

[37] J. Starck, Y. Moudden, and J. Bobin, "Polarized wavelets and curvelets on the sphere," *A&A*, vol. 497, pp. 931–943, Apr. 2009.

[38] M. Zaldarriaga and U. Seljak, "All-sky analysis of polarization in the microwave background," *PRD*, vol. 55, no. 4, pp. 1830–1840, Feb 1997.

[39] C. Durastanti, Y. Fantaye, F. Hansen, D. Marinucci, and I. Z. Pesenson, "Simple proposal for radial 3D needlets," *PRD*, vol. 90, no. 10, p. 103532, Nov. 2014.

[40] B. Leistedt and J. D. McEwen, "Exact wavelets on the ball," *IEEE TSP*, vol. 60, no. 12, pp. 6257–6269, 2012.

[41] J. D. McEwen and B. Leistedt, "Fourier-Laguerre transform, convolution and wavelets on the ball," in *10th International Conference on Sampling Theory and Applications (SampTA)*, 2013, pp. 329–333.

[42] F. Lanusse, A. Rassat, and J.-L. Starck, "Spherical 3D isotropic wavelets," *A&A*, vol. 540, p. A92, Apr. 2012.

[43] C. P. Ahn, R. Alexandroff, C. Allende Prieto, S. F. Anderson, T. Anderton, B. H. Andrews, É. Aubourg, S. Bailey, E. Balbinot, R. Barnes, and et al., "The Ninth Data Release of the Sloan Digital Sky Survey: First Spectroscopic Data from the SDSS-III Baryon Oscillation Spectroscopic Survey," *ApJ S.*, vol. 203, p. 21, Dec. 2012.

[44] J. D. McEwen, C. Durastanti, and Y. Wiaux, "Localisation of directional scale-discretised wavelets on the sphere," *ACHA, submitted*, 2015.

[45] E. J. Candès and D. L. Donoho, "Ridgelets: a key to higher-dimensional intermittency?" *Philosophical Transactions of the Royal Society of London A: Mathematical, Physical and Engineering Sciences*, vol. 357, no. 1760, pp. 2495–2509, 1999.

[46] E. Candès and D. Donoho, "Curvelets: A Surprisingly Effective Nonadaptive Representation of Objects with Edges," L. L. S. et al., Ed. Nashville, TN: Vanderbilt University Press, 1999.

[47] ——, "Continuous curvelet transform: I. resolution of the wavefront set," *ACHA*, vol. 19, no. 2, pp. 162–197, 2005.

[48] ——, "Continuous curvelet transform: Ii. discretization and frames," *ACHA*, vol. 19, no. 2, pp. 198–222, 2005.

[49] J. Radon, "Uber die bestimmung von funktionen durch ihre integralwerte lngs gewisser mannigfaltigkeiten," *Royal Saxonian Academy of Sciences*, vol. 69, pp. 262–277, 1917.

[50] ——, "On the determination of functions from their integral values along certain manifolds," *Medical Imaging, IEEE Transactions on*, vol. 5, no. 4, pp. 170–176, Dec 1986.

[51] P. Funk, "Uber eine geometrische anwendung der abelschen integralgleichung," *Math. Ann.*, vol. 77, pp. 129–135, 1916.

[52] D. S. Tuch, "Q-ball imaging," *Magn. Reson. Med.*, vol. 52, no. 6, pp. 1358–1372, 2004.

[53] A. W. Anderson, "Measurement of fiber orientation distributions using high angular resolution diffusion imaging," *Magnetic Resonance in Medicine*, vol. 54, no. 5, pp. 1194–1206, 2005.

[54] M. Descoteaux, E. Angelino, S. Fitzgibbons, and R. Deriche, "Regularized, fast, and robust analytical q-ball imaging," *Magnetic Resonance in Medicine*, vol. 58, no. 3, pp. 497–510, 2007.

[55] C. P. Hess, P. Mukherjee, E. T. Han, D. Xu, and D. B. Vigneron, "Q-ball reconstruction of multimodal fiber orientations using the spherical harmonic basis," *Magnetic Resonance in Medicine*, vol. 56, no. 1, pp. 104–117, 2006.

[56] L.-E. Andersson, "On the determination of a function from spherical averages," *SIAM Journal on Mathematical Analysis*, vol. 19, no. 1, pp. 214–232, 1988.

[57] J. Klein, "Inverting the spherical Radon transform for physically meaningful functions," *ArXiv Mathematics e-prints*, July 2003.

[58] A. K. Louis, M. Riplinger, M. Spiess, and E. Spodarev, "Inversion algorithms for the spherical radon and cosine transform," *Inverse Problems*, vol. 27, no. 3, p. 035015, 2011.

[59] R. Regnier, G. Rigaud, and M. Nguyen, "New approximated inversion of spherical radon transform in sar imaging," in *Image Processing (ICIP), 2013 20th IEEE International Conference on*, Sept 2013, pp. 2398–2401.

[60] J. Fadili and J.-L. Starck, "Curvelets and ridgelets," in *Computational Complexity*, R. A. Meyers, Ed. Springer New York, 2012, pp. 754–773.

[61] J. Ma and G. Plonka, "The curvelet transform," *IEEE Signal Processing Magazine*, vol. 27, no. 2, pp. 118–133, March 2010.

[62] K. M. Górski, E. Hivon, A. J. Banday, B. D. Wandelt, F. K. Hansen, M. Reinecke, and M. Bartelmann, "Healpix – a framework for high resolution discretization and fast analysis of data distributed on the sphere," *ApJ*, vol. 622, pp. 759–771, 2005.

[63] Y. Chan, J. D. McEwen, and Others, "Second-generation curvelets on the sphere," *in prep.*, 2015.

[64] O. Michailovich and Y. Rathi, "On approximation of orientation distributions by means of spherical ridgelets," *IEEE TIP*, vol. 19, no. 2, pp. 461–477, Feb 2010.

[65] ——, "Spatially regularized q-ball imaging using spherical ridgelets," in *Biomedical Imaging: From Nano to Macro, 2010 IEEE International Symposium on*, April 2010, pp. 1181–1184.

[66] E. T. Newman and R. Penrose, "Note on the Bondi-Metzner-Sachs group," *J. Math. Phys.*, vol. 7, no. 5, pp. 863–870, 1966.

[67] J. N. Goldberg, A. J. Macfarlane, E. T. Newman, F. Rohrlich, and E. C. G. Sudarshan, "Spin-s spherical harmonics and $\eth$," *J. Math. Phys.*, vol. 8, no. 11, pp. 2155–2161, 1967.

[68] D. A. Varshalovich, A. N. Moskalev, and V. K. Khersonskii, *Quantum theory of angular momentum*. Singapore: World Scientific, 1989.

[69] J. R. Driscoll and D. M. J. Healy, "Computing Fourier transforms and convolutions on the sphere," *Adv. Appl. Math.*, vol. 15, pp. 202–250, 1994.

[70] Y. Wiaux, L. Jacques, and P. Vandergheynst, "Fast spin ± 2 spherical harmonics transforms," *J. Comput. Phys.*, vol. 226, p. 2359, 2005.

[71] J. D. McEwen, "Fast, exact (but unstable) spin spherical harmonic transforms," *ARJ Phys.*, vol. 1, no. 1, 2011.

[72] J. D. McEwen and Y. Wiaux, "A novel sampling theorem on the sphere," *IEEE TSP*, vol. 59, no. 12, pp. 5876–5887, 2011.

[73] J. D. McEwen, M. Büttner, B. Leistedt, H. V. Peiris, and Y. Wiaux, "A novel sampling theorem on the rotation group," *IEEE SPL, submitted*, 2015.

[74] J. D. McEwen, M. P. Hobson, D. J. Mortlock, and A. N. Lasenby, "Fast directional continuous spherical wavelet transform algorithms," *IEEE TSP*, vol. 55, no. 2, pp. 520–529, 2007.

[75] B. D. Wandelt and K. M. Górski, "Fast convolution on the sphere," *PRD*, vol. 63, no. 12, p. 123002, 2001.

[76] Y. Wiaux, L. Jacques, P. Vielva, and P. Vandergheynst, "Fast directional correlation on the sphere with steerable filters," *ApJ*, vol. 652, pp. 820–832, 2006.

[77] P. Sadeghi, R. Kennedy, and Z. Khalid, "Commutative anisotropic convolution on the 2-sphere," *IEEE TSP*, vol. 60, no. 12, pp. 6697–6703, Dec 2012.

[78] R. Kakarala and P. Ogunbona, "A phase-sensitive approach to filtering on the sphere," *IEEE TSP*, vol. 60, no. 12, pp. 6330–6339, Dec 2012.

[79] D. C. Alexander, "Multiple-fiber reconstruction algorithms for diffusion mri," *Annals of the New York Academy of Sciences*, vol. 1064, no. 1, pp. 113–133, 2005.